

Cluster Simulation of the $O(N)$ loop model on the Honeycomb lattice

Youjin Deng *

Department of Physics, 4 Washington Square Place,
New York University, New York NY 10003, USA

Wenan Guo

Physics Department, Beijing Normal University,
Beijing 100875, People's Republic of China

Henk W.J. Blöte

Faculty of Applied Sciences, Delft University of Technology,
P.O. Box 5046, 2600 GA Delft, The Netherlands
Lorentz Institute, Leiden University,
P.O. Box 9506, 2300 RA Leiden, The Netherlands

February 6, 2008

Abstract

We study the $O(N)$ loop model on the Honeycomb lattice with real value $N \geq 1$ by means of a cluster algorithm. The formulation of the algorithm is based on the equivalence of the $O(N)$ loop model and the low-temperature graphical representation of a N -color Ashkin-Teller model on the triangular lattice. The latter model with integer N can be simulated by means of an embedding Swendsen-Wang-type cluster method. By taking into account the symmetry among loops of different colors, we develop another version of the Swendsen-Wang-type method. This version allows the number of colors N to take any real value $N \geq 1$. As an application,

*Correspondence should be sent to: yd10@nyu.edu

we investigate the $N = 1.25, 1.50, 1.75$, and 2 loop model at criticality. The determined values of various critical exponents are in excellent agreement with theoretical predictions. In particular, from quantities associated with half of the loops, we determine some critical exponents that corresponds to those for the tricritical $q = N^2$ Potts model but have not been observed yet. Dynamic scaling behavior of the algorithm is also analyzed. The numerical data strongly suggest that our cluster algorithm *hardly* suffers from critical slowing down.

1 Introduction

In Monte Carlo studies of statistical systems undergoing phase transitions, critical slowing down is one of the prominent problems. Consider a Monte Carlo algorithm with dynamic exponent $z > 0$. In order to generate a given number of effectively independent samples, one has to spend computing effort $\propto L^{d+z}$, where L is the linear system size and L^d accounts for the volume of the system of interest. For the local Metropolis algorithm for the Potts model, the dynamic exponent is around 2.2. Thus, in two dimensions, the required computing effort grows like $L^{4.2}$. Therefore, a central task of computational statistical physics is to develop algorithms such that z vanishes or is significantly suppressed. For a discussion of Monte Carlo methods, see Ref. [1].

For the Potts model, a significant breakthrough was the invention of the Swendsen-Wang cluster method [2] and its single-cluster version—the Wolff cluster method [3]. For the two- and three-dimensional Ising model, the dynamic exponent of the SW algorithm is about 0.1 and 0.45 [4], respectively. In comparison with the Metropolis simulations, the critical slowing down is significantly suppressed.

In addition to the Potts model, another important class of models in statistical physics is the $O(N)$ model. The $O(N)$ model is defined in terms of N -component spins on a lattice, with an isotropic pair coupling of the form $E_{ij} = \epsilon(\vec{S}_i \cdot \vec{S}_j)$, where i and j are a pair of neighboring lattice sites and ϵ is a function. A particularly interesting case is the honeycomb $O(N)$ model, where function ϵ is $\epsilon(p) \equiv -\log(1 + xp)$, with x a measure of the inverse temperature. It turns out that the $O(N)$ model has a nice graph representation [5–8]; the graph consists of a number of noninteracting and nonoverlapping loops on the honeycomb lattice.

However, in contrast to the Potts model, an efficient cluster algorithm is still lacking for the $O(N)$ model. When simulating the $O(N)$ model, one has to apply a Metropolis-like local algorithm, except for some special cases such as $N = 0$ or $N = 1$. Even worse is that local updates of loop configurations require some global connectivity information. Therefore, the computing effort grows like $L^{d+z+z'}$ as L increases, where the exponent z'

accounts for the effective critical slowing down due to the global-connectivity-checking procedure. The value of z' is close to 2 in two dimensions, unless some complicated data structure is applied.

Apart from the above computational considerations, developing efficient algorithms for the $O(N)$ loop model is also highly desirable from physical point of view. This is because, while much exact information about the critical properties of the $O(N)$ loop model has been accumulated in the past decades, many open questions still exist; for some recent publications, see e.g., Refs. [9–13]. As a generalization, dilution can be introduced into the $O(N)$ loop model and the Potts model. For a sufficient number of diluted sites, a different universality class can arise at the so-called tricritical point. In contrast to the tricritical Potts model, exact results for the tricritical $O(N)$ model are scarce. Therefore, a high-precision numerical study of the $O(N)$ model is of great importance.

In this work, we solved the long-standing problem of developing an efficient algorithm for the $O(N)$ loop model for $N \geq 1$. We apply the newly developed cluster algorithm, an embedding Swendsen-Wang-type cluster method, to the honeycomb $O(N)$ loop model without dilution, for which many exact predictions are available. The numerical data confirm the exact predictions by Coulomb gas theory and by conformal field theory. Further, the dynamical data imply that, for $N > 1$, the embedding cluster algorithm *hardly* suffers from critical slowing down.

2 The $O(N)$ loop and the Ashkin-Teller model: exact mapping

Let us consider a plane graph $\mathcal{G} = (V, E)$ and its dual graph $\mathcal{G}^* = (V^*, E^*)$. Let $|V|$ and $|E|$ denote the total numbers of vertices and of edges of \mathcal{G} , respectively, and $|V^*|$ and $|E^*|$ for graph \mathcal{G}^* . The dual relation between \mathcal{G} and \mathcal{G}^* guarantees $|E| = |E^*|$; there is one-to-one correspondence between edges of \mathcal{G} and \mathcal{G}^* .

On the edges of \mathcal{G} , bonds are placed such that they form a number of closed paths, or *loops*. In addition, it is required that these loops cannot share a common bond¹. The weight of such a loop configuration is given by $w^\ell N^c$, and the partition sum is

$$\mathcal{Z}_{\text{Loop}}(w, N) = \sum_{\text{loops}} w^\ell N^c, \quad (2.1)$$

where the sum is over all satisfied loop configurations. Symbol ℓ denotes the sum of the

¹Loops are allowed to intersect in the sense that they can share a common vertex.

lengths of all loops, and c is the number of loops. In principle, parameters w and N can be any real or complex numbers. In this work, we shall only consider real numbers $w > 0$ and $N > 0$, so that we have a probabilistic interpretation.

First, let us further restrict our attention to the case where $N \geq 1$ is an integer, and define a N -color Ashkin-Teller (AT) model [14, 15] on the dual graph \mathcal{G}^* ². On every vertex $i \in V^*$ of \mathcal{G}^* , one simultaneously places N independent Ising spins $\sigma^{(m)}$; say they have color $m = 1, 2, \dots, N$. On every edge $\langle i, \rangle \in E^*$, spins in the same color interact via couplings J_2 , and any two pairs of spins $\sigma^{(m)}$ and $\sigma^{(n)}$ that are in different colors interact via couplings J_4 . The latter involves four-spin interactions. The Hamiltonian reads

$$\mathcal{H}_{\text{AT}}(J_2, J_4, N) = -J_2 \sum_{m=1}^N \sum_{\langle i, \rangle \in E^*} \sigma_i^{(m)} \sigma_j^{(m)} - J_4 \sum_{m>n} \sum_{\langle i, \rangle \in E^*} \sigma_i^{(m)} \sigma_j^{(m)} \sigma_i^{(n)} \sigma_j^{(n)}. \quad (2.2)$$

The partition sum is then given by

$$\mathcal{Z}_{\text{AT}}(J_2, J_4, N) = \sum_{\{\sigma\}} e^{-\mathcal{H}_{\text{AT}}(\sigma)}, \quad (2.3)$$

where the sum is over all spin configurations $\sigma^{(m)}$ with $m = 1, 2, \dots, N$, as represented by a single symbol σ . Apparently, in the low-temperature region $J_2, J_4 \rightarrow \infty$, systems defined by Eq. (2.2) have N^2 ground states. The $N = 2$ case reduces to the isotropic version of the standard Ashkin-Teller model [14, 15].

In this work, we shall concentrate on model (2.2) in the infinite-coupling limit: $J_2 \rightarrow \infty$, $J_4 \rightarrow -\infty$, but $J_2 + (N-1)J_4 = J$ fixed at a finite value. In order to see the physical implication of this limit, let us consider the spin configurations on the ends of a given edge e of graph \mathcal{G}^* . From Eq. (2.2), if there are k unequal Ising variables in the same color on edge e , the Boltzmann weight reads

$$\begin{aligned} k=0 & : \quad \exp[J_2 N + \frac{1}{2} J_4 N(N-1)] \\ k=1 & : \quad \exp\{J_2(N-2) + \frac{1}{2} J_4[N(N-1) - 2(N-1)]\} \\ & \vdots \\ k & : \quad \exp\{J_2(N-2k) + \frac{1}{2} J_4[N(N-1) - 2k(N-1) + k(k-1)]\}. \end{aligned} \quad (2.4)$$

Normalizing these weights by that of case $k = 0$, one has Table 1.

²In Refs. [14, 15], only $N = 2$ was considered. Nevertheless, the Ashkin-Teller model with $N \neq 2$ has also received considerable research attentions; see e.g., Refs. [16, 17]

Configuration	Normalized weight
$k = 0$	1
$k = 1$	$e^{-2[J_2 + (N-1)J_4]} \equiv e^{-2J}$
$k \geq 2$	$e^{-2kJ} \cdot e^{k(k-1)J_4} \rightarrow 0$

Table 1: Boltzmann weights for the model (2.2) in the infinite-coupling limit. For any chosen two pairs of spins $\sigma^{(m)}$ and $\sigma^{(n)}$ with $m \neq n$ we first quote the weight read off from (2.2), and then the normalized weight obtained by making the first one equal to 1. We have used J to specify $J_2 + (N-1)J_4$. Notice that the weight for $k \geq 2$ vanishes.

In words, for any given edge $e \in E^*$, only two types of spin configurations are allowed on its ends: spins in the same color $\sigma_i^{(m)}$ and $\sigma_j^{(m)}$ are all equal, or there is *at most* one pair of unequal spins in the same color. The relative weight of the latter over the former is e^{-2J} . From now on, we shall refer to the AT model whose relative weights are given in Table 1 as the infinite-coupling AT model (IAT).

It turns out that, at least for integer N , the loop model defined by Eq. (2.1) can be exactly mapped onto the N -color IAT model. For this purpose, let us consider the low-temperature expansion of the IAT model, which can be performed in a similar way to the low-temperature expansion of Onsager's Ising model (see e.g., ref. [18]). For each color of Ising spin variable $\sigma^{(m)}$, we represent those unequal neighboring spins by lines of color m on the corresponding edge of the graph \mathcal{G} (recall that the IAT model itself is defined on the dual graph \mathcal{G}^*). In words, if two adjacent spins of color m are unequal, draw a line of color m on the edge of \mathcal{G} ; otherwise, do nothing. Do this for all pairs of nearest-neighbor spins. Apart from effects caused by boundaries ³, one obtains an Eulerian subgraph E' ; i.e., for every vertex, the number of lines touching it must be *even*. The lines are therefore joined together to form polygons (loops); these polygons have color m .

Conversely, these polygons divide the plane into spin-up and spin-down domains for Ising variable $\sigma^{(m)}$. For any such set of loops, there are just two corresponding spin configurations: they are related to each other by flipping all spins $\sigma^{(m)}$.

Do this for all colors of Ising variables σ (recall that we have used symbol σ to represent all spin variables $\sigma^{(m)}$ for $m = 1, 2, \dots, N$). One obtains a configuration containing N -color loops. Any such set of loops corresponds to N^2 spin configurations.

For the IAT model, the zero weight of configuration $\sigma_i^{(m)} \neq \sigma_j^{(m)}, \sigma_i^{(n)} \neq \sigma_j^{(n)}$ for any $m \neq n$ guarantees that there is at most one pair of unequal spins in same color on each

³One would expect that boundary effects vanish in the thermodynamic limit.

edge of \mathcal{G}^* . Therefore, although loops on graph \mathcal{G} can intersect, they can never share a common edge. An example of the low-temperature graph for the $N = 2$ IAT model on the triangular lattice is shown in Fig. 1.

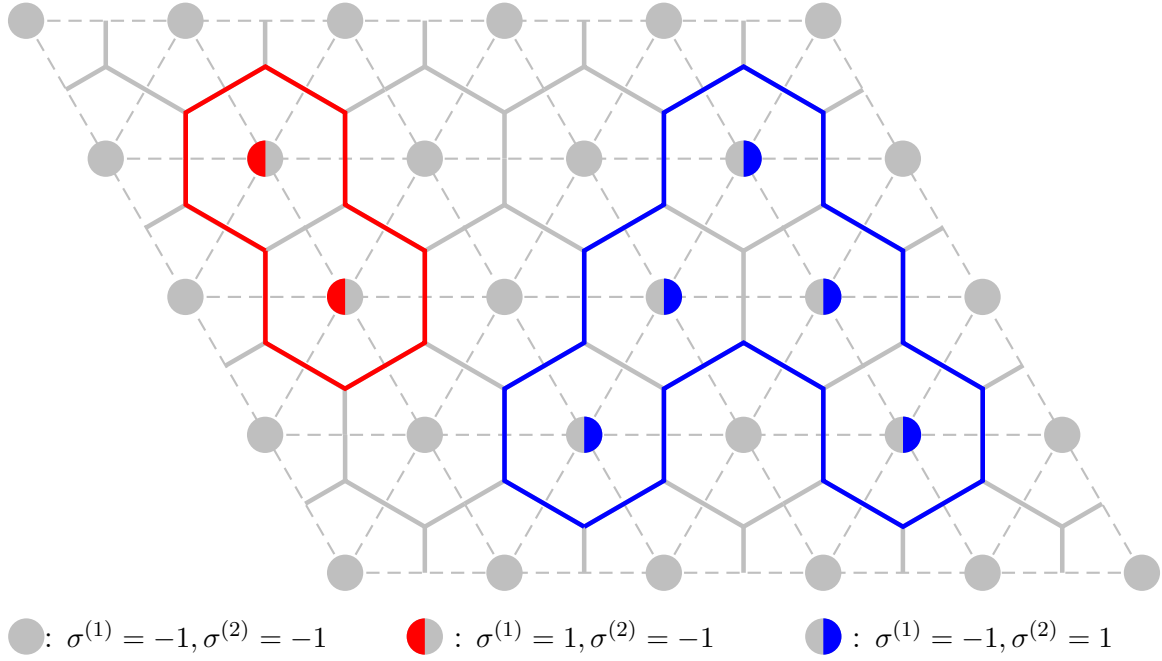


Figure 1: A low-temperature graph of the $N = 2$ IAT model on a triangular lattice of size 6×6 . The edges of the dual lattice – the honeycomb lattice, are shown as solid gray lines. Loops corresponding to Ising variables $\sigma^{(1)}$ and $\sigma^{(2)}$ are displayed as thick solid lines in red and in blue, respectively. No loops can intersect on the honeycomb lattice.

Let the energy of a ground state be zero. Table 1 tells that, in comparison with a ground state, a pair of unequal spins must receive an energy penalty e^{-2J} , denoted as w . The partition sum of the IAT model can then be written as

$$\mathcal{Z}_{\text{AT}}(J, N) = N^2 \sum_{\text{loops}} \sum_{\{\tau_i\}} w^{\ell_i} w^{\ell_j} \dots, \quad (2.5)$$

where the second sum is over all possible color arrangements for a given loop configuration. The factor N^2 accounts for the number of ground states. Note that each loop can randomly take one of the N colors with equal probability, and the second sum can then be easily evaluated. This leads to

$$\mathcal{Z}_{\text{AT}}(J, N) = N^2 \sum_{\text{loops}} w^{\ell} N^c, \quad (2.6)$$

where ℓ and c again represent the sum of the lengths of loops and the number of loops, respectively.

Apart from a trivial constant, the partition sum (2.6) is equal to Eq. (2.1). In other words, an exact one-to- N^2 mapping has been established between the loop model (2.1) and the N -color IAT model defined by Table 1. The weight w of the line segment in the loop configuration is related to J by $w = e^{-2J}$.

Note that, if the colors of loops are ignored, the loop representation of the IAT model is also a low-temperature graph of the Ising variable $s \equiv \prod_m \sigma^{(m)}$, the product of all N colors of variables $\sigma^{(m)}$. This observation is vital in the development of cluster algorithms for the $O(N)$ loop model, as shown later.

3 Cluster simulation of the AT model

Given the well-known Swendsen-Wang or Wolff cluster algorithm for Onsager's Ising model, an analogous cluster algorithm is readily available for the AT model described by Eq. (2.2)⁴. The so-called direct or embedding algorithms can be formulated. A detailed study of the Swendsen-Wang-type algorithms, including its dynamical behavior, was carried out by Salas and Sokal [20] in the context of the $N = 2$ AT model on the square lattice (not in the infinite-coupling limit). In the present work, we shall only consider the embedding version of the Swendsen-Wang-type algorithm.

For the AT model (2.2), for a given color of Ising variable $\sigma^{(m)}$, the effective Hamiltonian, conditioned on the other spin configurations $\sigma^{(n)}$ for $n = 1, 2, m-1, m+1, \dots, N$, can be written as

$$\mathcal{H}_{\text{eff}}(J_2, J_4, N; \sigma^{(m)}) = -J_{\text{eff}} \sum_{e \in E^*} \sigma_i^{(m)} \sigma_j^{(m)}, \quad (3.1)$$

where the effective nearest-neighbor coupling reads

$$J_{\text{eff}} = J_2 + J_4 \sum_{n \neq m} \sigma_i^{(n)} \sigma_j^{(n)}. \quad (3.2)$$

When all pairs of spins $\sigma_i^{(n)}$ and $\sigma_j^{(n)}$ for $n \neq m$ are equal, the effective interaction $J_{\text{eff}} = J_2 + (N-1)J_4 \equiv J$ is finite. Otherwise, one has the coupling $J_{\text{eff}} = J_2 + (N-1-2k)J_4 = J - 2kJ_4 \rightarrow \infty$. Thus, the effective coupling is no longer translation-invariant. Nevertheless, the effective coupling J_{eff} is always ferromagnetic. In this case, when the SW

⁴The word 'readily' here might seem misleading, since in some recent literature, the very inefficient Metropolis algorithm was still applied to simulate the standard Ashkin-Teller model in three dimensions, such as in Ref. [19].

cluster algorithm is applied to update the $\sigma^{(m)}$ spins, no frustration phenomena occur as in cluster simulation of the random Ising model. Therefore, it is plausible that the efficiency of such a cluster algorithm is not influenced too much by the inhomogeneous effective couplings.

A Swendsen-Wang step for updating a given Ising variable $\sigma^{(m)}$ can then be written as

- **Step 1: Place occupied bonds.** Given a spin configuration σ , for each edge $e \in E^*$ of \mathcal{G}^* , place an occupied bond with probability p

$$p = \begin{cases} 1 - e^{-2J} & \text{if } \sigma_i^{(m)} = \sigma_j^{(m)} \text{ and } \sigma_i^{(n)} = \sigma_j^{(n)} \text{ for all } n \neq m \\ 1 & \text{if } \sigma_i^{(m)} = \sigma_j^{(m)} \text{ and there is at least one pair } \sigma_i^{(n)} \neq \sigma_j^{(n)} \\ 0 & \text{if } \sigma_i^{(m)} \neq \sigma_j^{(m)}. \end{cases} \quad (3.3)$$

- **Step 2: Construct clusters.** Two vertices that are connected through a chain of occupied bonds are said to be in the same cluster. On the basis of occupied bonds, the whole set of vertices V^* of graph \mathcal{G}^* is decomposed into a number of clusters \mathcal{C} .
- **Step 3: Update spins $\sigma^{(m)}$.** For each cluster of \mathcal{C} , randomly assign the value of all spins on its vertices to be $+1$ or -1 with equal probability.

This completes a Swendsen-Wang cluster step for spin variable $\sigma^{(m)}$. Since all other spin variables $\sigma^{(n)}$ with $n \neq m$ are kept fixed, this cluster method is called an embedding cluster algorithm. We shall refer to this method as the embedding SW algorithm for the IAT model.

A valid embedding algorithm for the N -color AT model must involve the update of all colors of Ising spin variables σ . This can be done sequentially or randomly.

4 Cluster simulation of the $O(N)$ loop model

Owing to the exact mapping between the loop and the IAT model, for integer $N \geq 1$, the embedding method described in Sec. II is already a valid cluster algorithm for the $O(N)$ loop model on graph \mathcal{G} . In particular, for $N = 1$, this cluster method just reduces to the standard Swendsen-Wang cluster algorithm for the Ising model on graph \mathcal{G}^* . The procedure in Sec. II was already applied to simulate the $N = 2$ IAT model on the honeycomb, square, and triangular lattices [21]. In comparison with the Metropolis method, the critical slowing down is considerably suppressed, but still observable. At the critical point of the triangular IAT model, which corresponds both to the critical Baxter-Wu model and to the $O(2)$ loop model on the honeycomb lattice, it was found [21] that

the dynamical exponent z is about 1.18. In this section, we shall show that the cluster algorithm in Sec. II can be further improved such that it can simulate the loop model with noninteger $N \geq 1$ and that critical slowing down *hardly* exists.

Let us consider the Ising spin $s = \prod_m \sigma^{(m)}$. As mentioned earlier, any loop configuration of the $O(N)$ loop model on \mathcal{G} is also a low-temperature graph of the s -spin configurations on \mathcal{G}^* . But information about the colors of loops cannot be encoded in the s -spin configurations.

In terms of loop configurations, the simulation of $\sigma^{(m)}$ -spin variable in the embedding SW procedure in Sec. II is equivalently to update the loops of color m while keeping all other loops of color $n \neq m$ unchanged.

Our first task is then to rewrite the embedding SW procedure in Sec. II by using spin variable s and loop colors as the dynamical variables, instead of using $\sigma^{(m)}$ for $m = 1, 2, \dots, N$. This leads to the following four steps:

- **Step 1: Place occupied bonds.** Given a spin configuration s on \mathcal{G}^* and the color information for loops on \mathcal{G} , for each edge $e \in E^*$, place an occupied bond with probability p

$$p = \begin{cases} 1 - e^{-2J} & \text{if } s_i = s_j \\ 1 & \text{if } s_i \neq s_j \text{ and } e \text{ crosses a loop of color } n \neq m \\ 0 & \text{if } s_i \neq s_j \text{ and } e \text{ crosses a loop of color } m. \end{cases} \quad (4.1)$$

- **Step 2: Construct clusters** on the basis of occupied bonds. Note that the s spins on the vertices of a given cluster can have different signs.
- **Step 3: Update spins s .** For each cluster, flip all spins on its vertices with probability $1/2$.
- **Step 4: Update loops.** Consider the low-temperature graph of the s spin configuration, let the colors of the existing loops remain unchanged, and assign the color of all newly generated loops to be m .

Do Steps 1-4 for each of the N colors of loops. Step 4 is redundant for the procedure in Sec. II, since the colors of loops are already encoded in the spin configuration $\sigma^{(m)}$ with $m = 1, 2, \dots, N$.

For any satisfied loop configuration of the $O(N)$ loop model, the color of each loop can randomly take any value of N colors with equal probability. Therefore, instead of keeping all loop colors $n \neq m$ unchanged, one can randomly reassign the color of each loop in

Step 4, irrespective of the existing color information. On this basis, one can reformulate the embedding SW procedure as

- **Step 1: Construct loops and assign loop colors.** Given a spin configuration s on \mathcal{G}^* , construct the loop configuration on \mathcal{G} . For each loop, assign its color to be 1 with probability $1/N$ and to be 0 with probability $1 - 1/N$. We say loops of color 1 and 0 to be ‘active’ and ‘inactive’, respectively.
- **Step 2: Update the s -spin configuration.** This is done by the Swendsen-Wang-type procedure, in which the bond-occupation probability is

$$p = \begin{cases} 1 - e^{-2J} & \text{if } s_i = s_j \\ 1 & \text{if } s_i \neq s_j \text{ and } e \text{ crosses a loop of color 0} \\ 0 & \text{if } s_i \neq s_j \text{ and } e \text{ crosses a loop of color 1} \end{cases} \quad (4.2)$$

A cluster simulation of the $O(N)$ loop model can then be achieved by repeating the above two steps. Note that N is *no longer* required to be an integer; it is sufficient to demand that $N \geq 1$, since $1/N$ should not be bigger than 1.

In summary, in comparison with the embedding SW procedure described in Sec. II, the last version of the algorithm has two prominent features. First, N is no longer required to be an integer. Second, after a completion of the update of Ising spin variable, the loop colors are randomly reassigned, irrespective of the existing colors. This is possible because all the N colors of spin variables $\sigma^{(m)}$ ($m = 1, 2, \dots, N$) are symmetric to each other. In other words, the symmetry among the N -color spin variables is used in the last version of the embedding cluster algorithm. If this symmetry is broken in some way, e.g., one can let couplings J_2 depend on spin colors, the last version is then not applicable. But a slightly modified version of the procedure in Sec. II still works.

Because of usage of the symmetry among the N -color spin variables, one would expect that modes of the critical slowing down, associated with this symmetry, are significantly suppressed in the last version of the embedding SW algorithm. Thus, one expects that it is more efficient than the procedure in Sec. II. This will be numerically confirmed later.

Remark: For a plane graph \mathcal{G} of degrees $d > 3$, the loop assignment based on the s spin configuration is not unique, since loops are allowed to share a common vertex. Nevertheless, this should not affect the validity of the present embedding SW cluster algorithm.

We conclude this section by pointing out that our embedding SW cluster algorithm for the $O(N)$ loop model is of a similar spirit to the Chayes-Machta algorithm [22] for the q -state Potts model with real $q \geq 1$.

5 The Honeycomb $O(N)$ loop model

The Honeycomb lattice is of degree 3, and thus the loops of the $O(N)$ loop model never intersect. In this case, it has been known that the loop model can be exactly mapped on an $O(N)$ spin model with partition sum [6–8]

$$\mathcal{Z}(w, N) = \int \prod_k d\vec{S}_k \prod_{\langle ij \rangle \in E} (1 + w \vec{S}_i \cdot \vec{S}_j) , \quad (5.1)$$

where E is the edge set of the honeycomb lattice. Here, \vec{S} represents a N -dimensional unit vector – namely $|\vec{S}| = 1$ ⁵. This model has been under intensive investigation in the past two decades, and much exact information is available. For $N < 2$, the model undergoes a second-order phase transition; for $N = 2$, the transition is of infinite order–i.e., the so-called Kasteleyn-Thouless (KT) transition; for $N > 2$, it displays a lattice-gas-type transition. The renormalization exponents for critical $O(N)$ loop systems for $N \leq 2$ is a function of N . For $N > 2$, it is expected that the transition is in the same universality class of Baxter’s hard-hexagon lattice gas model on the triangular lattice (an exact mapping between the $N \rightarrow \infty$ loop model and the hard-hexagon lattice gas can be established).

The critical frontier for $N \leq 2$ is exactly located at [7, 8]

$$w_c(N) = \left(2 + \sqrt{2 - N}\right)^{-1/2} . \quad (5.2)$$

It was observed [7, 8] that a *critical* $O(N)$ model corresponds with a *tricritical* $q = N^2$ -state Potts model. From exact calculations, conformal field theory [23], and Coulomb gas theory [8], exact values of renormalization exponents can be obtained for the tricritical Potts model as

$$\begin{aligned} y_{t1} &= 3 - \frac{6}{g} \\ y_{t2} &= 4 - \frac{16}{g} \\ y_{t3} &= 5 - \frac{30}{g} \\ y_{h1} &= 2 - \frac{(6 - g)(g - 2)}{8g} \\ y_{h2} &= 2 - \frac{(10 - g)(g + 2)}{8g} , \end{aligned} \quad (5.3)$$

⁵In Ref. [7], the $O(N)$ spin model is defined such that $|\vec{S}| = \sqrt{N}$ and the factor w is replaced by λ/N

where the Coulomb-gas couplings g is related to q as

$$g = 4 + \frac{2 \arccos\left(\frac{q-2}{2}\right)}{\pi} . \quad (5.4)$$

The symbols y_{t1} , y_{t2} , and y_{t3} represent exponents of the leading, subleading, and next-subleading thermal scaling fields, respectively, and y_{h1} and y_{h2} are for the magnetic scaling fields. Therefore, exact values of critical exponents for the $O(N)$ model described by Eq. (5.1) as a function of N are also known.

6 Simulation and Sampled quantities

We applied the embedding SW cluster algorithm in Sec. III to simulate the $O(N)$ loop model on the honeycomb lattice; the Ising variable s is defined on the vertices of the dual lattice—i.e., the triangular lattice. The sampled quantities can be classified into three types; they are associated with loop configurations, Ising spin variables, and distributions of clusters \mathcal{C} formed in the SW step.

The first type includes the total lengths of loops and of the number of loops, as normalized by the volume of the system V and denoted by ρ_l and ρ_c , respectively. Here, the volume V is the total number of vertices on the corresponding triangular lattice. The second-moment fluctuations of ρ_l are also sampled as $C = V(\langle \rho_l^2 \rangle - \langle \rho_l \rangle^2)$, where symbol $\langle \rangle$ represents the statistical average.

Taking into account the mapping between the loop model and the IAT model, we also measured both the total lengths and the number of ‘active’ loops, denoted by ρ_{la} and ρ_{ca} ; the fluctuations of ρ_{la} , denoted as C_a , were also measured. The subscript ‘a’ means ‘active’.

The second type of quantities concern the Ising variables associated with loop configurations. A natural quantity to sample is the magnetic susceptibility $\chi = V\langle m^2 \rangle$, where m is the magnetization density for spin variable s . After each embedding SW step, we also reconstructed Ising spins $\sigma^{(1)}$ from these active loops. The associated susceptibility χ_a was then sampled. In addition, we consider the size distribution of domains enclosed by those active loops. These domains can be obtained by placing occupied bonds between all equal nearest-neighbor $\sigma^{(1)}$ Ising spins. They are named the Ising clusters in the standard Ising model. We measured the second moment of these Ising clusters

$$S_{2a} = \frac{1}{V^2} \sum_i a_i^2 , \quad (6.1)$$

where a_i is the number of $\sigma^{(1)}$ spins in the i th domain.

The last type of quantities contains information for the embedding SW simulations. They include the number of occupied bonds per spin n_b , the number of clusters per spin n_c , and the second and fourth moment of cluster sizes

$$W_k = \frac{1}{V^k} \sum_i c_i^k, \quad (6.2)$$

where $k = 2$ or 4 , and c_i is the size of the i th cluster formed in the embedding SW simulations.

In the conventional SW simulation of the Ising model (or more generally of the Potts model), quantities W_2 and W_4 are exactly related to the second and the fourth moment of the magnetization density. The bond-number density is also exactly related to the energy density in the Ising model.

On the basis of the above sampled quantities, we sampled ratios

$$Q = \frac{\langle \chi \rangle^2}{\langle \chi^2 \rangle}, \quad Q_a = \frac{\langle \chi^{(1)} \rangle^2}{\langle \chi^{(1)2} \rangle}, \quad \text{and} \quad Q_w = \frac{\langle W_2 \rangle^2}{\langle 3W_2^2 - 2W_4 \rangle}. \quad (6.3)$$

At criticality, these amplitudes ratios are dimensionless and universal. They are known to be very useful in locating critical points in Monte Carlo studies of statistical systems undergoing phase transitions. For the SW simulation of the Ising model, quantity Q_w reduces to Q defined on the basis of magnetic susceptibility.

6.1 Test of the algorithm

For a test of the algorithm, we performed simulations for $N = 1.5$ and $N = 1.9$. The system sizes took 12 values in range $8 \leq L \leq 256$, where L is the linear system size of the triangular lattice. Periodic boundary conditions were applied. Measurements were taken after every Swendsen-Wang step.

For $N = 1.5$, Eq. (5.2) yields the critical point at $J_c = -(\ln w_c)/2 = 0.24897\dots$. Simulations were performed in range $0.245 \leq J \leq 0.253$. About 6×10^6 samples were taken for each size L . Parts of the Q data are shown in Fig. 2. The intersections of the Q data for different system sizes rapidly converge to the expected value $J_c = 0.24897\dots$. This implies the validity of the embedding cluster algorithm for the $O(N)$ loop model with noninteger N .

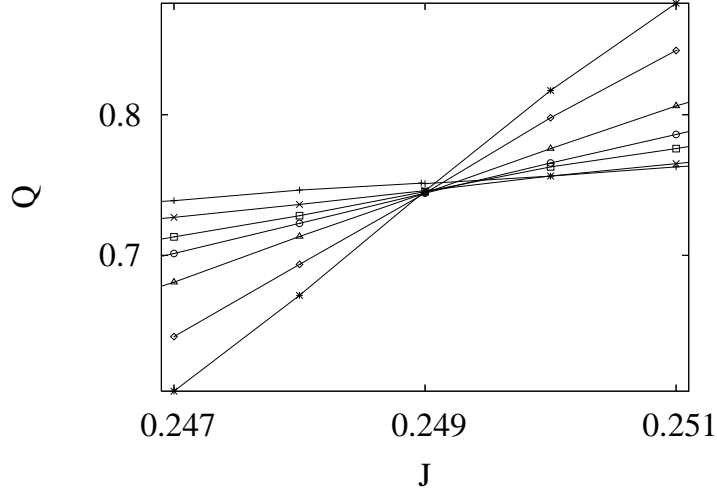


Figure 2: Binder ratio Q for $N = 1.5$. The data points $+$, \times , \square , \circ , \triangle , \diamond , and $*$ represent system sizes $L = 8, 16, 32, 48, 80, 160$, and 256 , respectively. The error bars of the data are smaller than the point sizes. The lines, which simply connect data points for each L , are just for illustration.

According to the least-squares criterion, we fitted the Q data by

$$Q(J, L) = Q_c + \sum_{k=1}^m (J - J_c)^k L^{ky_t} + b_i L^{y_i} + b_1 L^{y_1} + \dots, \quad (6.4)$$

where $m > 1$ is an integer. The terms with amplitudes b_i and b_1 describe finite-size corrections. The term with exponent y_i is supposed to arise from the leading irrelevant scaling field. Thus, the value of y_i is given by y_{t3} in Eq. (5.3). For $N = 1.5$, Eq. (5.3) yields $y_i \equiv y_{t3} = -1.097296$. Other finite-size corrections can arise from various sources, such as from the subleading irrelevant scaling field, from the analytical part of the free energy f , and from the second derivative of f with respect to the leading irrelevant field. It is not *a priori* clear how many or which such correction terms can be observed in the numerical data. Thus, one should make various fits by taking into account all possible sources of finite-size corrections. Final estimates of interested quantities are then obtained by comparing the results of various fits. We let exponent y_t and y_i to be fitted by the numerical data, and fixed y_1 at -2 for simplicity. All the Q data in range $8 \leq L \leq 256$ can be successfully described by Eq. (6.4). The results are $y_t = 0.749(4)$, $y_i = -1.4(3)$, $J_c = 0.24896(2)$, and $Q_c = 0.7429(8)$. The value of y_t is consistent with the exact value $y_{t2} = 0.7481 \dots$ in Eq. (5.3), and that of y_i agrees with $-1.097 \dots$. The estimated critical

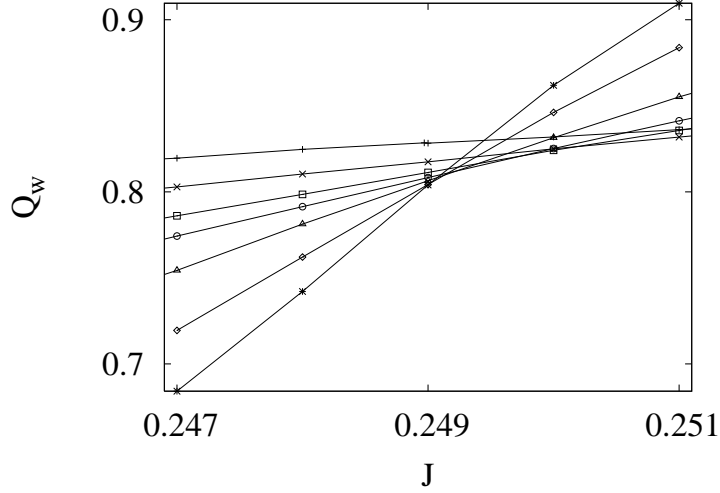


Figure 3: Binder ratio Q_w for $N = 1.5$. The data points $+$, \times , \square , \circ , \triangle , \diamond , and $*$ represent system sizes $L = 8, 16, 32, 48, 80, 160$, and 256 , respectively. The error bars of the data are smaller than the point sizes. The lines, which simply connect data points for each L , are just for illustration purpose.

point is also in excellent agreement with the exact prediction $0.24897\dots$.

Next, we plotted parts of the Q_w data in Fig. 3. The intersections of the Q_w data reflect the percolation threshold of clusters formed in the embedding SW procedure. In cluster simulations of statistical systems, the efficiency can be reflected by the average size of the formed clusters. The efficiency will be limited if the average size is either too small or too big: little change of configurations is made for the former, and large amount of effort has to be carried out for the latter (probably it also accompanies by little change). Ideally, the percolation threshold of clusters formed in Monte Carlo simulations should coincide or be very close to the phase transition of statistical systems. This is indeed the case in the present embedding SW algorithm for the $O(N)$ loop model, as reflected by Fig. 3.

The fits of the $Q_w(L)$ data by Eq. (6.4) yields $y_t = 0.756(6)$, $y_i = -1.2(3)$, and $J_c = 0.24900(3)$. The estimated percolation threshold is consistent with the thermal critical point $J_c = 0.24897\dots$.

We also simulated the $N = 1.9$ loop model. Equation (5.2) predicts the critical point at $J_c = 0.20998\dots$. Simulations were performed in range $0.206 \leq J \leq 0.214$, and system sizes took 12 values in range $8 \leq L \leq 256$. Parts of the Q data are shown in Fig. 4. As expected, the intersections of the Q data for different sizes converge rapidly to

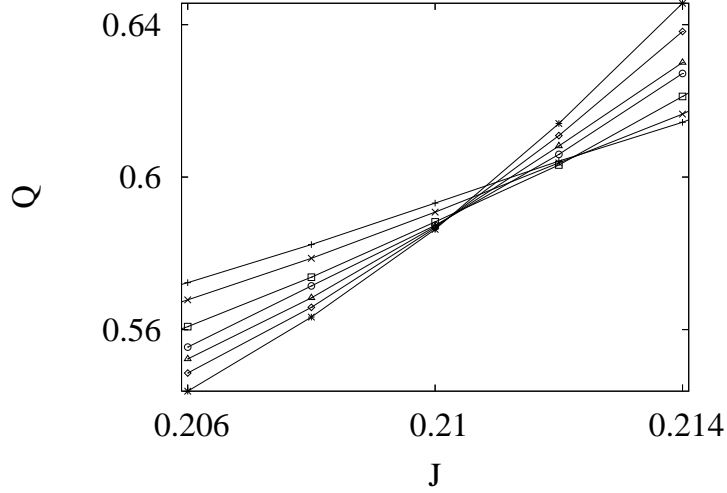


Figure 4: Binder ratio Q for $N = 1.9$. The data points $+$, \times , \square , \bigcirc , \triangle , \diamond , and $*$ represent system sizes $L = 8, 16, 32, 48, 80, 160$, and 256 , respectively. The error bars of the data are smaller than the point sizes. The lines, which simply connect data points for each L , are just for illustration purpose.

$J_c = 0.20998 \dots$. The fits of the Q data by Eq. (6.4) yields $y_t = 0.373(6)$, $y_i = -1.2(2)$, $J_c = 0.21000(8) \approx 0.20998 \dots$, and $Q_c = 0.586(1)$. The value of y_t is more or less consistent with that of $y_{t2} = 0.367 \dots$. But that of y_i does not agree with that of $y_{t3} = -1.81 \dots$. In this case, we expect that the dominant finite-size corrections are not described by exponent y_{t3} .

A plausible scenario for the dominant finite-size corrections might be the following. As mentioned earlier, the mapping between the $O(N)$ model on graph \mathcal{G} and the IAT model on the dual graph \mathcal{G}^* is only exact up to boundary effects. Even though these boundary effects are expected to vanish in the thermodynamic limit $L \rightarrow \infty$, they cannot be neglected for finite L . According to a simple argument, these boundary effects vanish as a function of $1/L$. Indeed, exponent -1 is consistent with the numerical values of y_i for $N = 1.5$ and $N = 1.9$.

7 Simulation at criticality

For $N = 1.25, 1.5, 1.75$, and 2 , we performed extensive simulations right at the exactly predicted critical points given by Eq. (5.2). Periodic boundary conditions were applied, and the system sizes took 18 values in range $4 \leq L \leq 1024$. Samples were taken after

every embedding SW step. The number of samples is 10^7 for $L \leq 256$, and 2×10^6 for $L > 256$ (Wenan and Henk: Monte Carlo data are not complete yet).

For later convenience, we list in Table. 2 the exact values of critical exponents for $N = 1, 1.25, 1.50, 1.75$, and 2 , as predicted by Eq. (5.3); also included are the exact values of critical points given by Eq. (5.2).

N	y_{t1}	y_{t2}	y_{t3}	y_{h1}	y_{h2}	J_c
1	1.875	1	-0.625	1.9479...	1.1979...	0.274653...
1.25	1.8327...	0.8873...	-0.8361...	1.9343...	1.1562...	0.263231...
1.50	1.7805...	0.7481...	-1.0972...	1.9198...	1.1069...	0.248970...
1.75	1.7078...	0.5542...	-1.4607...	1.9034...	1.0420...	0.229072...
2.00	1.5	0	-2.5	1.875	0.875	0.173286...

Table 2: Exact values of critical points and exponents for $N = 1, 1.25, 1.75, 2$, as predicted by Eqs. (5.2) and (5.3).

7.1 $N = 2$: KT point

The critical $N = 2$ loop model on the honeycomb lattice is a very special case. It can be mapped both onto the standard $N = 2$ IAT model on the triangular lattice and the Baxter-Wu model with three-spin interactions on the triangular lattice. The latter has been exactly solved by various methods, and is believed to be in the same universality class as the 4-state Potts model. Further, it is known that the $N = 2$ loop model undergoes a KT transition, which is an infinite-order phase transition.

Energy-like quantities. The energy-like quantities include the density of the length of loops ρ_l and of the loop number ρ_c . The exact information for the critical properties of the $O(2)$ model tells one that, at criticality, the finite-size behavior of ρ_l and ρ_c is governed by the subleading thermal exponent y_{t2} in Eq. (5.3). From the analysis of Monte Carlo data, as shown later, it turns out that the finite-size scaling behavior of bond-occupation density n_b , a quantity associated with the embedding SW step, is also described by y_{t2} . Instead of being listed in tables, the ρ_l and ρ_c data are shown in Fig. 5; the vertical axis shows the data for $\rho_l(L) - \rho_{l0}$, $\rho_c(L) - \rho_{c0}$, and $n_b(L) - n_{b0}$, where constants ρ_{l0} , ρ_{c0} , and n_{b0} were obtained from the numerical fits.

We made a least-squares fit of the Monte Carlo data for energy-density-like quantities

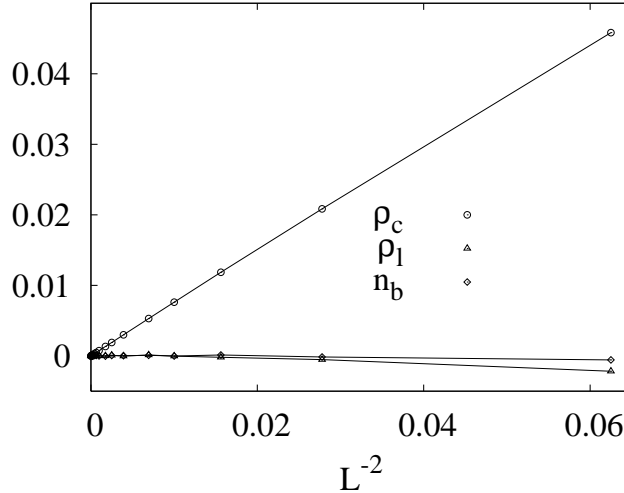


Figure 5: Quantities ρ_l , ρ_c , and n_b for $N = 2$. In order to display the finite-size dependence for different quantities, the analytical-background contributions in these quantities have been subtracted. Namely, the data in the vertical axis are $\rho_l(L) - \rho_{l0}$, $\rho_c(L) - \rho_{c0}$, and $n_b(L) - n_{b0}$, where $\rho_{l0} = 1.114835(4)$, $\rho_{c0} = 0.0574189(7)$, and $n_{b0} = 1.10956(2)$ were obtained from fits by Eq. (7.1). The exponent -2 of L in the horizontal axis is $y_{t2} - 2$.

to the general ansatz

$$E(L) = E_0 + L^{y_t-d}(a + b_0 L^{-1} + b_i L^{y_i} + \dots) . \quad (7.1)$$

The symbols E and E_0 should be replaced by specific quantities in the fits. For instance, depending on which quantity is going to be analyzed, E can be ρ_l , ρ_c , and n_b , and E_0 can be ρ_{l0} , ρ_{c0} , and n_{b0} .

In Eq. (7.1), the term with b_0 describes boundary effects arising from the mapping between the Ising-spin configuration and the loop representation. The term with b_i arises from the least irrelevant scaling field. However, the value of y_i is not very clear. According to conformal field theory, if an operator with exponent y exists, a sequence of exponents $y - 1$, $y - 2$, \dots , can in principle also exist. Therefore, y_i can be y_{t3} or $y_{t2} - 1$ etc. In the analysis of our Monte Carlo data, we have tried to take into account all possible sources of finite-size corrections.

The fits yield $y_t = 0.1(2)$ and $\rho_{l0} = 1.114835(4)$ for the $\rho_l(L)$ data, $y_t = 0.004(8)$ and $\rho_{c0} = 0.057418(7)$ for the $\rho_c(L)$ data, and $y_t = -0.5(10)$ and $n_{b0} = 1.10956(2)$ for the $n_b(L)$ data. The values of y_t are all in good agreement with the prediction $y_{t2} = 0$.

Within the sampled quantities, the density of the lengths and of the number of active

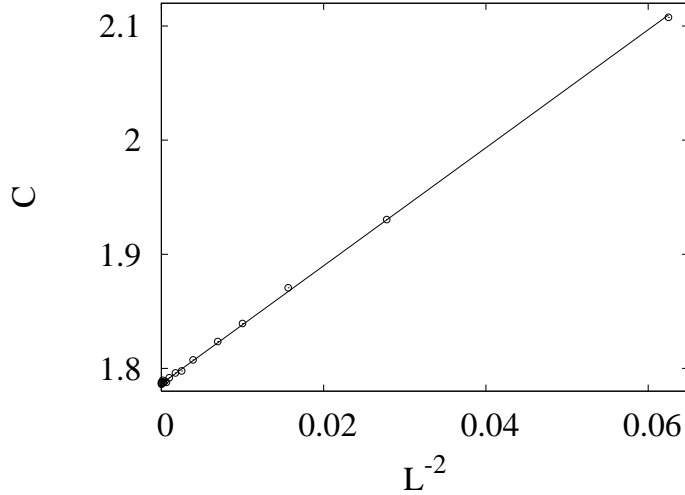


Figure 6: Specific-heat-like quantity C for $N = 2$. The exponent -2 of L in the horizontal axis is equal to $2y_{t2} - 2$.

loops, ρ_{la} and ρ_{ci} , are also energy-like quantities. Since the color of each loop can randomly take one of N colors, the statistical mean value of $\rho_{la}(L)$ is just $\rho_c(L)/N$ for any size L ; the same applies to quantity ρ_c . Therefore, we do not need to analyze them.

Specific-heat-like quantities. Quantities C and C_a account for the fluctuations of ρ_l and ρ_{la} , respectively. The C and C_a data are respectively shown in Figs. 6 and 7. These suggest that the finite-size behavior of C is governed by exponent $2y_{t2} - 2 = -2$, while that of C_a is governed by $2y_{t1} - 2 = 1$.

An observation is that the behavior of the magnetic susceptibility χ , for the $s = \prod \sigma^{(m)}$ for $m = 1, 2, \dots, N$, is also described by exponent $2y_{t1} - 2 = 1$. Actually, for the present case $N = 2$, because of the symmetry between two Ising variables $\sigma^{(1)}$ and $\sigma^{(2)}$ for the IAT model, it can be shown that, in the thermodynamic limit $L \rightarrow \infty$, $C_a(L)$ and $\chi(L)$ are equivalent to each other (Wenan Henk: this statement has not been carefully checked).

The data for specific-heat-like quantities were fitted by

$$\mathcal{C}(L) = \mathcal{C}_0 + L^{2y_t-d}(a + b_0 L^{-1} + b_i L^{y_i} + \dots), \quad (7.2)$$

where symbols \mathcal{C} and \mathcal{C}_0 should be replaced by specific quantities in the fits.

The fits of the $C(L)$ data yield $y_t = -0.01(3) = y_{t2}$ and $C_0 = 1.7867(8)$, and those of C_a give $y_t = 1.5002(4) = y_{t1}$ and $C_{a0} = -0.46(3)$.

Susceptibility-like quantities. Quantity χ for the s Ising variable has been dis-

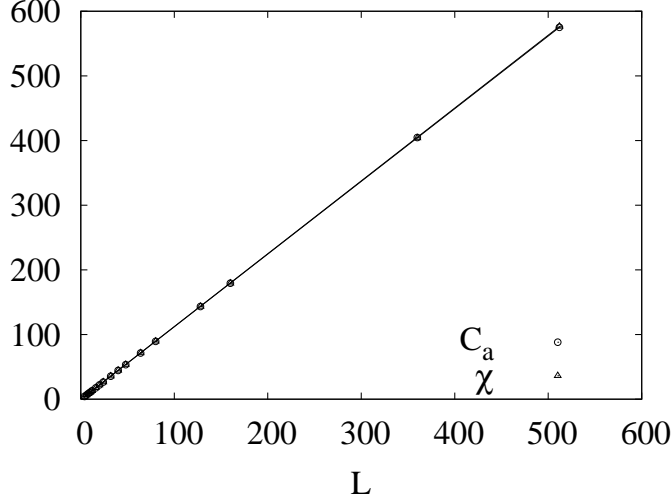


Figure 7: Quantities C_a and χ for $N = 2$. The exponent 1 of L in the horizontal axis is equal to $2y_{t1} - 2$. In this scale, the $C_a(L)$ and $\chi(L)$ data collapse for each L .

cussed earlier. The fits of the $\chi(L)$ data also yield $y_t = 1.5002(4) = y_{t1}$. Other susceptibility-like quantities include χ_a for spin $\sigma^{(1)}$, S_{2a} for the Ising clusters of spin variable $\sigma^{(1)}$, and W_2 for the clusters formed in the embedding SW step. The data of these quantities are shown in Figs. 8 and 9.

The data for susceptibility-like quantities were fitted by

$$\mathcal{K}(L) = \mathcal{K}_0 + L^{2y_h - d}(a + b_0 L^{-1} + b_i L^{y_i} + \dots), \quad (7.3)$$

where symbols \mathcal{K} and \mathcal{K}_0 should be replaced by specific quantities in the fits. Exponent y_h is left to be fitted by numerical data.

The fits of the $\chi_a(L)$ and $W_2(L)$ data by Eq. (7.3) yield $y_h = 1.8751(1)$ and $y_h = 1.8751(2)$, respectively. Both results are in good agreement with the exact value of $y_{h1} = 15/8 = 1.875$, as given in Table 2. This implies that the percolation threshold of the clusters formed in the embedding SW step coincides with the thermal critical point $J_c(N = 2) = \ln 2/4$.

The fit of S_{2a} yield $y_h = 1.9444(1)$. There is no prediction of the exact value for this exponent.

Binder ratios. In the Monte Carlo simulations, we also sampled dimensionless amplitude ratios Q and Q_a , defined by Eq. (6.3). The Q and Q_a data are shown in Fig. 10.

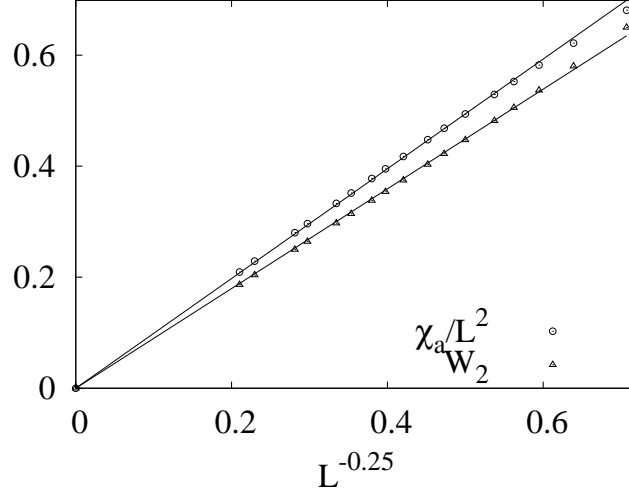


Figure 8: Susceptibility-like quantities χ_a/L^2 and W_2 for $N = 2$. The exponent $-1/8$ of L in the horizontal axis is equal to $2y_{h1} - 4$.

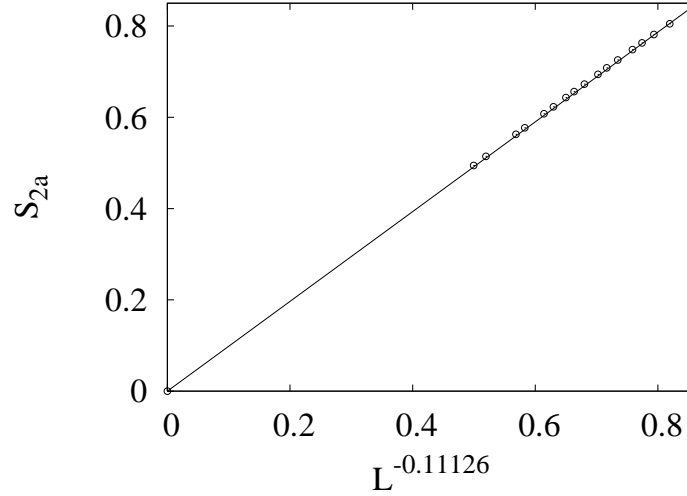


Figure 9: Quantity S_{2a} for $N = 2$. The exponent -0.11126 of L in the horizontal axis is obtained from the fits.

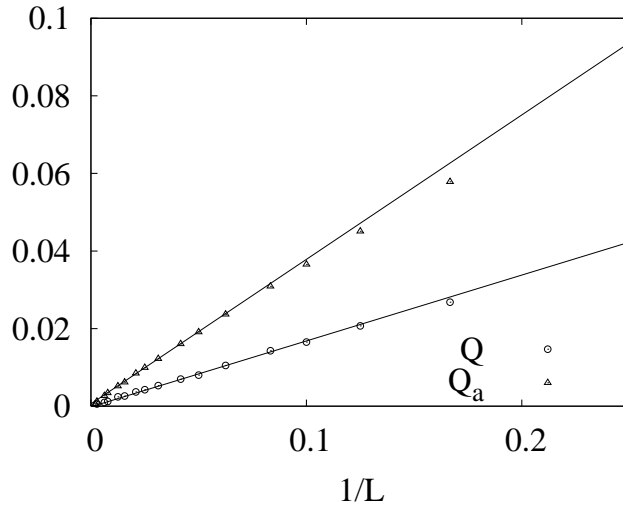


Figure 10: Ratios Q and Q_a for $N = 2$. The exponent -1 of L in the horizontal axis is can be explained as $y_{t2} - 1$; it is also in good agreement with the fitting results for Q and Q_a .

The data for amplitude ratios were fitted by

$$\mathcal{Q}(L) = \mathcal{Q}_0 + b_i L^{y_i} + \dots, \quad (7.4)$$

where exponent y_i is left to be determined by numerical data. The fits of the $Q(L)$ data yield $Q_0 = 0.4774(4)$ and $y_i = -1.03(6)$, and those of Q_a give $Q_{a0} = 0.6927(4)$ and $y_i = -0.99(3)$. Both estimates of y_i agree with integer -1 , which can be explained as $y_{t2} - 1$.

7.2 $N = 1.25, 1.50$, and 1.75

The analysis of the Monte Carlo data for the honeycomb $O(N)$ model with $N = 1.25, 1.50$, and 1.75 follows an analogous procedure as that for $N = 2$. Thus, the details of the fitting procedure are skipped here. The fitting results are listed in Tables 3 and 4.

For $N = 2$, quantities associated with those active loops or the spin variable $\sigma^{(1)}$ have clear physical meaning, since they appear naturally in the $N = 2$ IAT model described by Eq. (2.2). In this case, the scaling behavior of specific-heat-like quantity C_a and susceptibility χ_a can be predicted from the exact results for the Baxter-Wu model or for the triangular IAT model. The numerical results fit well with the predictions. Nevertheless,

N		ρ_l	ρ_c	n_b	C	C_a
1.25	y	0.887(2)	0.884(5)	0.885(5)	0.885(4)	1.378(3)
	$y(\text{exact})$	0.887...	0.887...	0.887...	0.887...	—
	r	0.61297(2)	0.040207(2)	1.09962(2)	8.9(1)	2.7(2)
1.5	y	0.745(3)	0.74(1)	0.75(2)	0.74(1)	1.406(2)
	$y(\text{exact})$	0.748...	0.748...	0.748...	0.748...	—
	r	0.72952(2)	0.046245(2)	1.13371(2)	4.8(2)	1.21(4)
1.75	y	0.54(1)	0.54(1)	0.50(5)	0.57(4)	1.432(3)
	$y(\text{exact})$	0.554...	0.554...	0.554...	0.554...	—
	r	0.86058(1)	0.051884(2)	1.15514(2)	3.160(6)	0.7(9)
2.00	y	0.1(2)	0.004(8)	−0.5(10)	−0.01(3)	1.5002(4)
	$y(\text{exact})$	0	0	0	0	1.5
	r	1.114835(4)	0.057418(7)	1.10956(2)	1.7867(8)	−0.46(3)

Table 3: Fitting results for energy-associated quantities. Symbol r represents those analytical contributions, arising from the regular part of the free energy. Also included are the predicted values for exponent y to be fitted. Symbol “—” means that no prediction exists.

no exact results seem to exist for the finite-size behavior of the geometric quantity S_{2a} , the second-moment of the Ising clusters for spin $\sigma^{(1)}$.

For noninteger N , however, the symmetry between the active and the inactive loops breaks. To our knowledge, there are thus far no prediction for exponents governing the scaling behavior of quantities C_a and χ_a , as listed in Tables 3 and 4. On the other hand, the following scenario seems plausible. The estimated exponent y for C_a in Table 3 is actually the mixed effect of y_{t1} and y_{t2} , while that for χ_a is due to the effective mixture of y_{h1} and y_{h2} . We did try to make fits for the C_a and χ_a by taking into account such a mixture effect, but the results seem worse than those by Eqs. (7.2) and (7.3).

An observation is that, independent of the N value, the exponents for the scaling behavior of χ_a and W_2 are always equivalent. This strongly suggests that the percolation threshold of clusters formed in the embedding SW step coincides with the thermal critical point for any $N \geq 1$. A rigorous proof is lacking.

N		χ	χ_a	W_2	S_{2a}	Q	Q_a
1.25	y	1.8327(2)	1.8806(3)	1.8804(3)	1.9491(2)	-1.6(2)	-0.56(6)
	$y(\text{exact})$	1.8327...	—	—	—	-1.09...	—
	Q					0.8069(2)	0.8245(7)
1.5	y	1.7801(4)	1.8843(2)	1.8841(2)	1.9499(1)	-1.1(2)	-0.60(4)
	$y(\text{exact})$	1.7805...	—	—	—	-1.09...	—
	Q					0.7426(4)	0.7931(4)
1.75	y	1.7079(4)	1.8854(2)	1.8854(1)	1.9497(1)	-1.6(2)	-0.79(8)
	$y(\text{exact})$	1.7078...	—	—	—	-1.46...	—
	Q					0.6585(2)	0.7628(4)
2.00	y	1.5004(5)	1.8751(1)	1.8751(2)	1.9444(1)	-1.03(6)	-0.99(3)
	$y(\text{exact})$	1.5	1.875	1.875	—	-1?	-1?
	Q					0.4774(4)	0.6927(4)

Table 4: Fitting results for susceptibility-associated quantities. Symbol Q represents the universal values of those amplitude ratios at criticality. We also give the predicted values for exponent y to be fitted. The exponent y for amplitude ratios is for the dominant finite-size corrections. The question mark means that we are not very sure about the prediction of y_i .

8 Dynamical behavior

During the Monte Carlo simulations, the value of every sampled quantity was saved on hard disk after every sweep. Statistical analyses were then performed on these data. Both static and dynamic information of sampled quantities can then be obtained.

Let symbol f be a given quantity, the unnormalized autocorrelation function is then defined as

$$C_f(t) \equiv \langle f(0)f(t) \rangle - \langle f \rangle^2. \quad (8.1)$$

The normalized autocorrelation function is

$$\rho_f(t) \equiv C_f(t)/C_f(0). \quad (8.2)$$

Typically, $\rho(t)$ decays exponentially ($\sim e^{-|t|/\tau}$) for large t , and the exponential autocor-

relation time is defined as

$$\tau_{exp,f} = \lim_{t \rightarrow \infty} \sup \frac{t}{-\ln |\rho_f(t)|} . \quad (8.3)$$

In addition, we define the integrated autocorrelation time

$$\tau_{int,f} = \frac{1}{2} \sum_{t=-\infty}^{\infty} \rho_f(t) = \frac{1}{2} + \sum_{t=1}^{\infty} \rho_f(t) . \quad (8.4)$$

Here, the factor 1/2 is purely a matter of convention; it follows the definition in Ref. [24]. The integrated autocorrelation time controls the statistical error in Monte Carlo measurements of $\langle f \rangle$. More precisely, the sample mean has variance

$$\text{var}(\bar{f}) \approx \frac{1}{n} (2\tau_{int,f}) C_f(0) \quad \text{for } n \gg \tau, \quad (8.5)$$

where n is the total length of Monte Carlo simulations.

8.1 $N = 2$

Parts of the numerical data for the normalized autocorrelation function are shown in Fig 11 for susceptibility χ , in Fig. 12 the density of loop lengths ρ_l , and in Fig. 13 for susceptibility χ_a for spin variable $\sigma^{(1)}$. The good collapse of the ρ data strongly suggests that the critical slowing down is *absent* in the embedding SW simulation of the $O(2)$ loop model on the honeycomb lattice.

For quantity χ_a , after a single Monte Carlo step, the autocorrelation function drops to a value smaller 0.1. This means that two subsequent samples are almost effectively independent.

Except for very small t , the data lines in Figs.11, 12, and 13 are rather straight; the scattering phenomena at the right-hand side are due to statistical noise. Therefore, the autocorrelation function is almost a purely exponential function of time: $\rho \approx e^{-t/\tau}$.

The integrated autocorrelation time τ_{int} defined in Eq. (8.4) was also measured for all sampled observables. Apart from the constant factor 1/2, quantity τ_{int} is just the area under the ρ data line as a function of time t . Parts of the τ_{int} data are shown in Fig. 14.

We fitted the τ_{int} data for the sampled quantities by

$$\tau_{int}(L) = \tau_0 + L^z (b_1 + b_2 L^{-1} + \dots) , \quad (8.6)$$

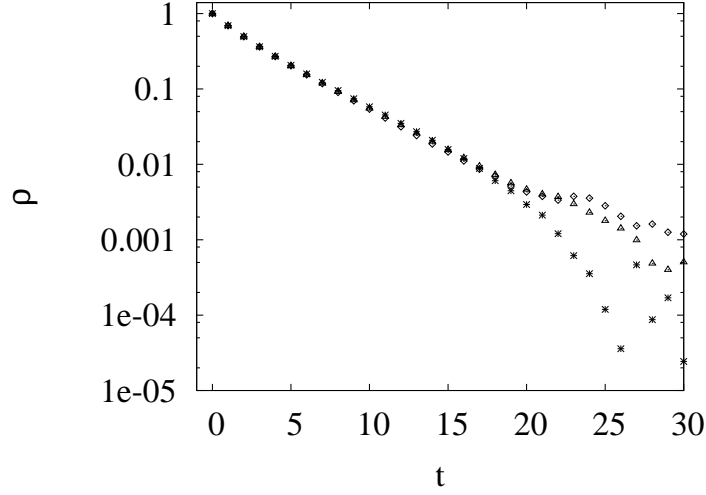


Figure 11: Normalized autocorrelation function ρ for susceptibility χ . The data points \triangle , \diamond , and $*$ are for system sizes $L = 160, 256, 360$, and 512 , respectively. The scattering behavior at the right-hand side is due to statistical noise. For $\rho_\chi \geq 0.01$, the ρ data for different system sizes collapse rather well in this scale. This suggests that the critical slowing down is absent in our embedding SW simulations of the $O(2)$ loop model on the honeycomb lattice.

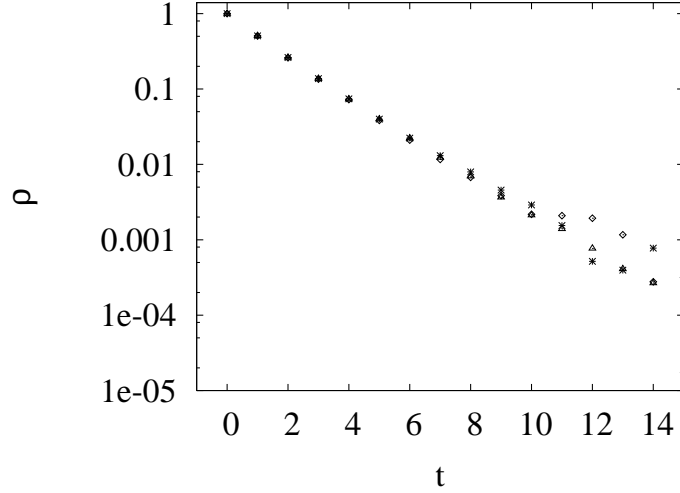


Figure 12: Normalized autocorrelation function ρ for the density of loop lengths ρ_l . The data points \triangle , \diamond , and $*$ are for system sizes $L = 160, 256, 360$, and 512 , respectively. The scattering behavior at the right-hand side is due to statistical noise. For $\rho_\chi \geq 0.01$, the ρ data for different system sizes collapse rather well in this scale. This suggests that the critical slowing down is absent in our embedding SW simulations of the $O(2)$ loop model on the honeycomb lattice.

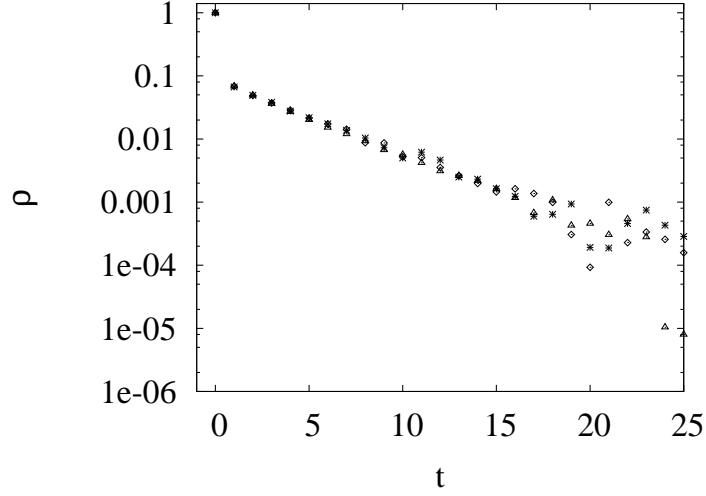


Figure 13: Normalized autocorrelation function ρ for susceptibility χ_a corresponding Isin spin variable $\sigma^{(1)}$. The data points \triangle , \diamond , and $*$ are for system sizes $L = 160, 256, 360$, and 512 , respectively. The scattering behavior at the right-hand side is due to statistical noise. For $\rho_\chi \geq 0.01$, the ρ data for different system sizes collapse rather well in this scale. This suggests that the critical slowing down is absent in our embedding SW simulations of the $O(2)$ loop model on the honeycomb lattice.

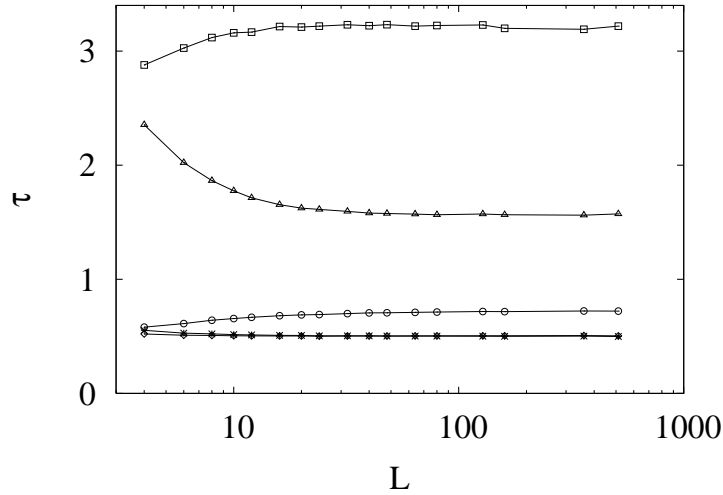


Figure 14: Integrated autocorrelation time τ_{int} for $N = 2$. The data points \square , \circ , \triangle , \diamond , and $*$ are for susceptibility χ , susceptibility χ_a for active spins, density of loop lengths ρ_l , the second moment W_2 of the clusters formed in Monte Carlo steps, and the bond-occupation density n_b , respectively. For the last two quantities, τ_{int} is very close to 0.5 , which means that autocorrelation function $\rho(t)$ is essentially zero for $t > 0$.

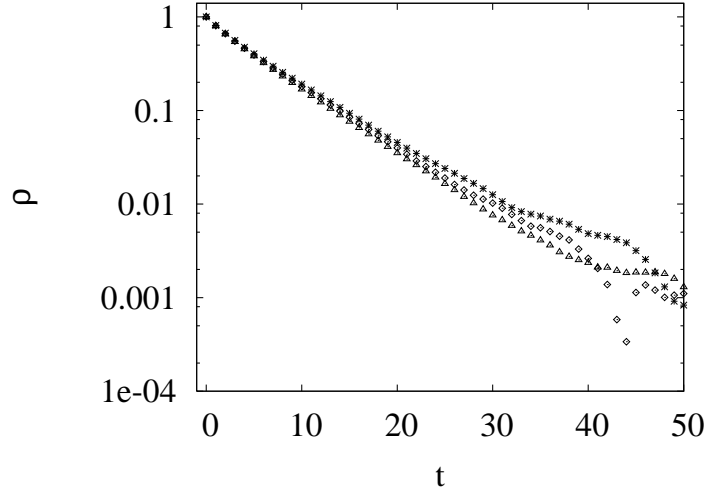


Figure 15: Autocorrelation function ρ_{ρ_l} for $N = 1.25$. The data points \triangle , \diamond , and $*$ are for system sizes $L = 160, 256, 360$, and 512 , respectively. The scattering behavior at the right-hand side is due to statistical noise.

where the dynamic exponent z is left free to be determined by the numerical data. We assume that correction exponent -1 , which appears in static quantities, also exists in the dynamical data. Nevertheless, it turns out that, for $L \geq 8$, all the τ_{int} data for quantities in Fig. 14 can be fitted by Eq. (8.6) with $b_2 = 0$. The results are shown in Table 5. These show that, for all quantities shown in Table 5, the integrated autocorrelation time τ_{int} converge rapidly to constants as $L \rightarrow \infty$; the values of these constants are all rather small. Quantity χ has the largest autocorrelation time τ_{int} , and ρ_l has the next largest τ_{int} .

8.2 $N = 1.25, 1.50$ and 1.75

For $N = 1.25, 1.50$ and 1.75 , the general behavior of ρ and τ for quantities listed in Table 5 is similar as that for $N = 2$. Namely, the autocorrelation function $\rho(t)$ is almost a purely exponential function of time t . For quantity χ_a , after a single Monte Carlo step, the value of ρ drops to a significantly small value, which is about 0.27 for $N = 1.25$. The quantities that have the largest two values of correlation time τ_{int} are χ and ρ_l ; ρ_l has the largest value for $N = 1.25$ and χ for the others. Therefore, we only show the ρ_l data for $N = 1.25$ in Fig. 15 and the χ data for $N = 1.50$ and 1.75 in Figs. 16 and 17, respectively.

The τ_{int} data for the quantities in Table 5 are also shown in Figs. 18, 19 and 20 for

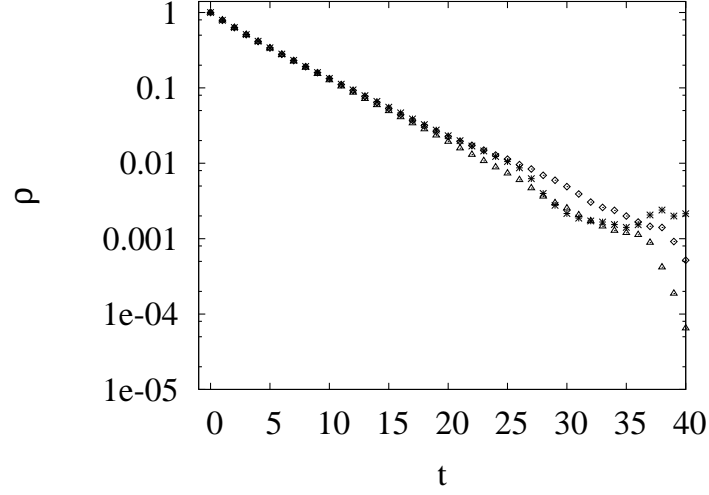


Figure 16: Autocorrelation function ρ_χ for $N = 1.50$. The data points \triangle , \diamond , and $*$ are for system sizes $L = 160, 256, 360$, and 512 , respectively. The scattering behavior at the right-hand side is due to statistical noise.

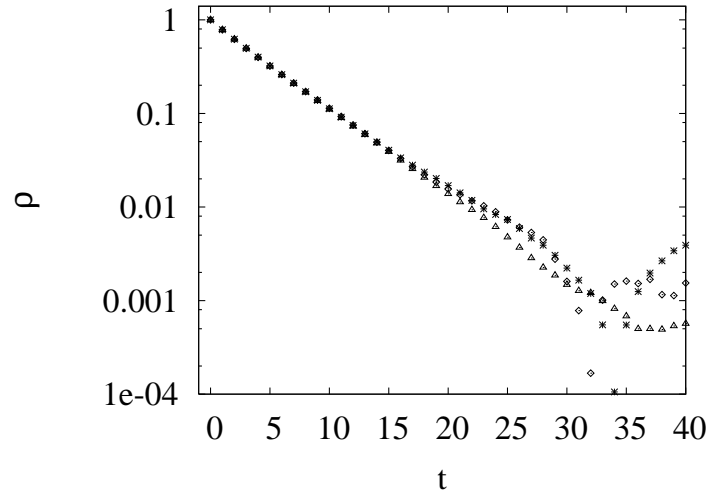


Figure 17: Autocorrelation function ρ_χ for $N = 1.75$. The data points \triangle , \diamond , and $*$ are for system sizes $L = 160, 256, 360$, and 512 , respectively. The scattering behavior at the right-hand side is due to statistical noise.

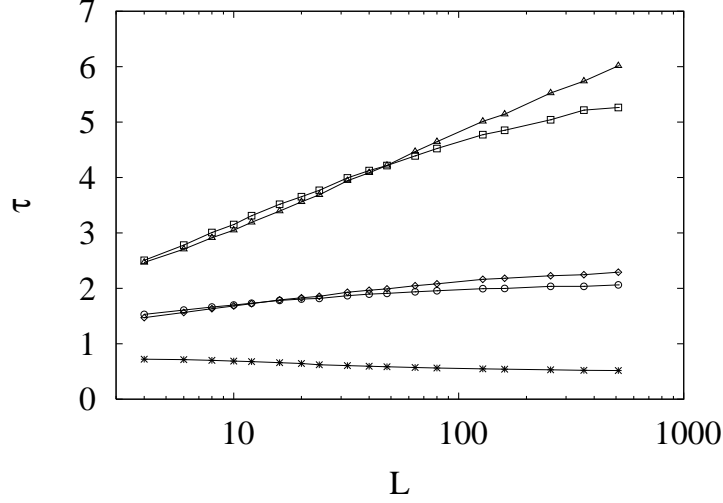


Figure 18: Integrated autocorrelation time τ_{int} for $N = 1.25$. The data points \square , \circ , \triangle , \diamond , and $*$ are for χ , χ_a , ρ_l , W_2 and n_b , respectively.

$N = 1.25, 1.50$, and 1.75 , respectively.

From Fig. 18 for $N = 1.25$, it is not completely clear whether the critical slowing down is absent or not for quantities ρ_l and χ . Nevertheless, the approximately straight line of quantity ρ_l suggests that, even the critical slowing down exists, the integrated correlation time τ may diverge in a logarithmic format or in a power law of L with a very small exponent z .

We fitted the τ_{int} data by Eq. (8.6). For the τ_{int,ρ_l} data for $N = 1.25$, it turns out they can still be described by Eq. (8.6) when a correction term with b_2 is also included. For the other quantities and for the other values N , the τ_{int} data for $L \geq 8$ all can be well described by Eq. (8.6) with $b = 0$. The results are shown in Table 5; the value of b_1 is $2.5(8)$ for τ_{int,ρ_l} with $N = 1.25$.

Taking into account the approximate linearity of the τ_{int,ρ_l} data for $N = 1.25$ in Fig. 18, we also fitted the τ_{int,ρ_l} data by

$$\tau_{int}(L) = \tau_0 + \tau_i \ln L + b_1 L^{-1}. \quad (8.7)$$

Indeed, all the data can be well described by Eq. (8.7); we obtain $\tau_0 = 1.17(4)$, $\tau_i = 0.79(2)$, and $b_1 = 0.8(2)$.

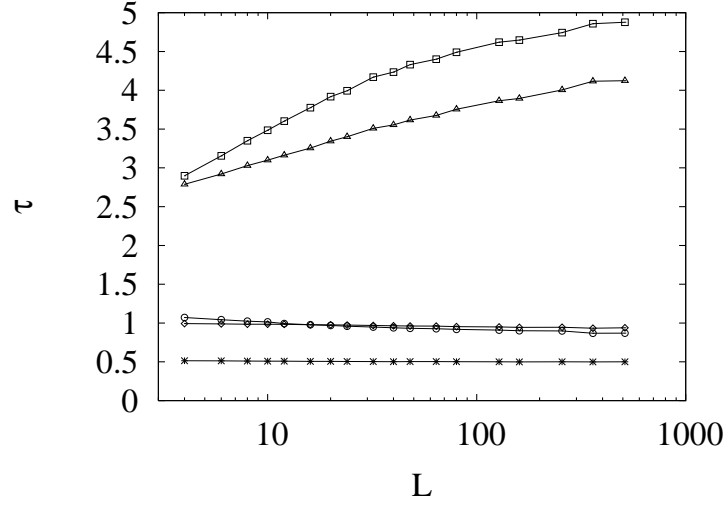


Figure 19: Integrated autocorrelation time τ_{int} for $N = 1.25$. The data points \square , \circ , \triangle , \diamond , and $*$ are for χ , χ_a , ρ_l , W_2 and n_b , respectively.

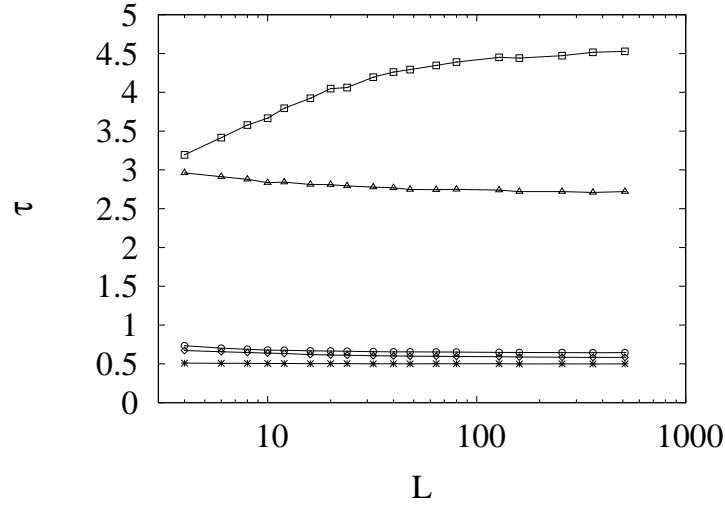


Figure 20: Integrated autocorrelation time τ_{int} for $N = 1.25$. The data points \square , \circ , \triangle , \diamond , and $*$ are for χ , χ_a , ρ_l , W_2 and n_b , respectively.

Quantity		$N = 1.25$	$N = 1.50$	$N = 1.75$	$N = 2.00$
ρ_l	τ_0	18(4)	5.2(3)	2.70(2)	1.566(3)
	z	-0.06(2)	-0.17(2)	-0.60(7)	-1.7(1)
χ	τ_0	7.7(2)	5.18(10)	4.55(3)	3.221(6)
	z	-0.17(2)	-0.43(3)	-0.80(7)	-2.3(3)
χ_a	τ_0	2.18(2)	0.82(3)	0.640(2)	0.722(2)
	z	-0.36(2)	-0.28(4)	-0.64(8)	-0.94(6)
n_b	τ_0	0.499(4)	0.498(4)	0.500(1)	0.5002(4)
	z	-0.65(3)	-0.6(1)	-0.8(1)	-1.2(2)
W_2	τ_0	2.7(1)	0.92(1)	0.577(3)	0.5036(8)
	z	-0.23(3)	-0.42(4)	-0.54(6)	-2.6(8)

Table 5: Fitting results for the integrated autocorrelation time τ_{int} .

9 Discussion

By making use of the equivalence of the loop configurations of the $O(N)$ loop model and the low-temperature graph of the Ashkin-Teller model in the infinite-coupling limit (IAT), we formulated an embedding Swendsen-Wang-type algorithm for the $O(N)$ loop model with real value $N \geq 1$. For $N = 1$, this algorithm reduces to the conventional Swendsen-Wang method for the Ising model. With some modifications, an embedding Wolff-type method (single-cluster version) is readily available.

We then applied our cluster algorithm to the $O(N)$ loop model on the honeycomb lattice. The numerical data reveal the finite-size scaling behavior of several quantities. The associated exponents are confirmed to be those exact values predicted by the Coulomb gas theory and by conformal field theory.

The dynamical data strongly imply that the embedding cluster algorithm suffers little from critical slowing down. This is somewhat impressive in the sense that the dynamic exponent z of the Swendsen-Wang type algorithm must satisfy the Li-Sokal bound [25]: $z \geq \alpha/\nu$, unless it can be proved that the amplitude of terms with exponent α/ν vanishes. The value of $\alpha/\nu \equiv 2y_{t1} - 2$ can be easily calculated from Eq. (5.3), which yields $1.6654 \dots$, $1.5610 \dots$, 1.4156 , and 1 for $N = 1.25, 1.50, 1.75$, and 2 , respectively. The absence of a dynamic exponent $z > \alpha/\nu$ in the embedding SW simulations of the $O(N)$ loop model implies that the amplitude for terms with exponent α/ν indeed vanishes. We argue that this is because our embedding SW cluster algorithm has made use of the symmetry among the N colors of Ising spins.

Similar scenarios exist elsewhere. For instance, it can be proved that, in Metropolis simulations of the Ising model, the dynamic exponent z must satisfy $z \geq \gamma/\nu$. However,

the dynamic exponent z of the Swendsen-Wang algorithm is much smaller than γ/ν . This is because the symmetry between the up- and down-pointing Ising spins is fully taken into account in the Swendsen-Wang algorithm.

To have a better understanding of our above argument, let us consider another version of Swendsen-Wang-type cluster method for the IAT or the $O(N)$ model with integer N , as described in Sec. II. This algorithm directly simulates each color of the spin variables $\sigma^{(m)}$ in the IAT model for $N = 1, 2, \dots, N$. In the language of loop configurations, the algorithm only updates loops in the same color; it does not interchange or reassign colors of loops. In other words, the symmetry among loops in different colors is not taken into account. Such a cluster algorithm has been applied to the critical $N = 2$ IAT model on the triangular lattice, which is equivalent to the critical $O(2)$ model on the honeycomb lattice or the Baxter-Wu model. It was found that the dynamic exponent z for the integrated correlation time is 1.18(2); indeed, z satisfies the Li-Sokal bound: $z > \alpha/\nu$.

Instead of the individual spin variables $\sigma^{(m)}$, the final version of the embedding SW algorithm simulates the product variable $s = \prod \sigma^{(m)}$. After each update of spin variable s , the colors of loops are reassigned randomly, irrespective of the existing colors of loops. In this sense, it is natural that dynamic exponent $z \geq \alpha/\nu$ vanishes.

One would then expect that the subleading exponent $\alpha'/\nu = 2y_{t2} - 2$ serve as a lower bound for the dynamic exponent of our embedding SW cluster algorithm.

The $N = 1$ loop model is just the Ising model. From universality, one has $\alpha'/\nu \equiv 2y_{t2} - 2 = 0$ for the $O(1)$ model on any planar graph. On the honeycomb lattice, Eqs. (5.3) and (5.4) tell that α'/ν is a monotonically decreasing function of $q = N^2$. Therefore, one has $\alpha'/\nu < 0$ for $N > 1$. In this sense, our cluster algorithm still satisfies the Li-Sokal bound. Since the value of α'/ν decreases as a function of N , it is also expected that, as N increases, the value of τ_{int} decrease. This is consistent with τ_0 in Table 5.

It is clear from Sec. III that the embedding cluster algorithm described in this work cannot be applied to the $N < 1$ case. Nevertheless, since all the loop configurations are the low-temperature graphs of the s spin variable, and vice versa. It seems that, for $N \approx 1$, a reweighting modification of the Swendsen-Wang simulation of the Ising model can still be useful. Such a procedure can be described as

- **Step 1.** For a spin configuration $\{s\}$, in which the number of loops is c , generate a new spin configuration $\{s'\}$ by using the Swendsen-Wang algorithm.
- **Step 2.** Derive the loop information for the new configuration $\{s'\}$, and calculate the loop number c' . Accept the new configuration with probability $N^{c'-c}$, namely, set $s \leftarrow s'$. Otherwise, keep the old spin configuration s .

Repeating of these two steps forms a valid ‘cluster’ algorithm for $N \leq 1$. For the $O(N)$ loop model on the honeycomb lattice, it turns out that, for $N \geq 0.8$ and small system sizes $L \leq 100$, this algorithm works pretty well.

References

- [1] K. Binder and D. Stauffer, *Applications of the Monte Carlo Method in Statistical Physics* (Springer-Verlad, Berlin, 1984).
- [2] R.H. Swendsen and J.-S. Wang, Phys. Rev. Lett. **58**, 86 (1987).
- [3] U. Wolff, Phys. Rev. Lett. **62**, 361 (1989).
- [4] G. Ossola and A.D. Sokal, Nucl. Phys. B **691**, 259 (2004).
- [5] H.E. Stanley, Phys. Rev. Lett. **20**, 589 (1968).
- [6] E. Domany, D. Mukamel, B. Nienhuis, and A. Schwimmer, Nucl. Phys. B **190**, 279 (1981).
- [7] B. Nienhuis, Phys. Rev. Lett. **49**, 1062 (1982).
- [8] B. Nienhuis, J. Stat. Phys. **34**, 731 (1984).
- [9] L. Chayes, L.P. Pryadko, and K. Shtengel, Nucl. Phys. B **570**, 590 (2000).
- [10] W. Guo, H.W.J. Blöte, and F.Y. Wu, Phys. Rev. Lett. **85**, 3874 (2000).
- [11] J.L. Jacobsen, N. Read, and H. Saleur, Phys. Rev. Lett. **90**, 090601 (2003).
- [12] W. Janke and A.M.J. Schakel, Phys. Rev. Lett. **95**, 135792 (2005).
- [13] W. Guo, B. Nienhuis, and H.W.J. Blöte, Phys. Rev. Lett. **96**, 045704 (2006).
- [14] J. Ashkin and E. Teller, Phys. Rev. **64**, 178 (1943).
- [15] C. Fan, Phys. Lett. A **39**, 136 (1972).
- [16] G.S. Grest and M. Widom, Phys. Rev. B **24**, 6508 (1981).
- [17] E. Fradkin, Phys. Rev. Lett. **53**, 1967 (1984).
- [18] R.J. Baxter, *Exactly Solved Models in Statistical Mechanics* (Academic Press, London–New York, 1982).

- [19] G. Musial, L. Debski, and G. Kamieniarz, Phys. Rev. B **66**, 012407 (2002).
- [20] J. Salas, and A.D. Sokal, J. Stat. Phys. **87**, 1 (1997).
- [21] Y. Deng, J. Salas, T. Garoni, A. Sportiello, and A.D. Sokal, unpublished.
- [22] L. Chayes and J. Machta, Physica A **254**, 477 (1998).
- [23] J.L. Cardy, *Phase Transitions and Critical Phenomena*, edited by C. Domb and J.L. Lebowitz. (Academic Press, London, 1987), Vol. 11, p. 55, and references therein.
- [24] A.D. Sokal, *Monte Carlo Methods in Statistical Mechanics: Foundations and New Algorithms*, lecture notes at the Cargèse Summer School, 1996.
- [25] X.-J. Li and A.D. Sokal, Phys. Rev. Lett. **63**, 827 (1989).

